Channel Measurements and Modeling for Low Terahertz Communications in an Aircraft Cabin

Tobias Doeker, *Graduate Student Member, IEEE*, Johannes M. Eckhardt, *Graduate Student Member, IEEE*, and Thomas Kürner, *Fellow, IEEE*

***Abstract*— The low terahertz band (0.1–1 THz) offers very high data rates for novel mobile applications and constitutes a promising candidate to meet the requirements in aviation, enabling future wireless in-flight entertainment (IFE) systems. An extensive knowledge of the propagation effects in the radio channel in complex scenarios is a prerequisite to successfully design a communication system. This article presents a measurement campaign in a real aircraft investigating the radio channel at 300 GHz for different deployments of a wireless IFE system. The propagation effects as well as temporal and spatial channel characteristics are analyzed for likely communication links between an access point and a user equipment (UE). In the same way, interference links between two UEs are studied, reporting transmission and reflection losses for various components of the aircraft. A deterministic and geometry-based channel model is derived and extended to cover the effect of human blockage that suggests an integration of the access point into the passenger service unit. The measurement and realistic path loss models can be used in further link and system level simulations and contribute to the design of future IFE systems.**

***Index Terms*— 300 GHz, aircraft, channel, channel sounding, in-flight entertainment (IFE), modeling, propagation, terahertz (THz).**

I. Introduction

THE constant growing market of mobile subscribers and the growth in the number of personal electronic devices (PEDs) per user connected to the Internet [1] illustrate the importance of PEDs in nowadays society. Transferred to aviation, this trend entails that passengers expect to be able to use their PEDs during a flight. The ability to use one's own device increases the comfort of the passengers drastically [2]. Especially for business traveler, an airline would enhance the passenger experience by enabling the possibility of working unrestrictedly during the flight. To enable the change from a centralized toward a personnel in-flight entertainment (IFE), an easy access of the user equipment (UE) to the Internet and entertainment system must be given, motivating a wireless IFE system solution.

Besides the passenger, the airline also benefits from a wireless IFE system as it allows for a rapid reconfiguration of the cabin's seating [3]. Furthermore, the disadvantage of sensitive connectors in a wired IFE system could be avoided. One of the major aspects optimizing an aircraft is the reduction of weight. Here, the wireless IFE benefits from the usage of passengers' PEDs which makes the integrated screens redundant. Therefore, the removal of the screens and cables reduces the weight of the aircraft [4].

Nowadays, most IFE systems are still wire-based and only seldom systems based on WiFi are integrated. Nevertheless, research activities investigating the radio channel in the ultra wide-band (UWB) range (up to a few 10 GHz) within an aircraft cabin have been started already several years ago [5]–[7]. Promising larger bandwidth to cover higher data rates, characteristics at 60 GHz with focus on blockage by human bodies also have been analyzed [8], [9]. However, only line-of-sight (LOS) conditions are investigated and reflections in the aircraft are not especially considered. Extending the 60 GHz approach, a solution based on the IEEE 802.15.3c standard [2] is also reported, but it presents a system approach and does not investigate further propagation aspects within the aircraft cabin. Besides that, a visible light communication (VLC) based solution is introduced using the reading lights [10]. However, this approach requires a LOS link between the transmitter (TX) and the receiver (RX) and continuous lighting, probably impractical during night flights. In addition to that, a communication system through the seat rails [4] is reported, but the proposed systems could not provide the data rates needed for a satisfactory connection for hundreds of passengers in a low-weight and cost-efficient way [11]. Therefore, the low terahertz (THz) band is a promising solution for the wireless connection between the access point (AP) and the UE.

The low THz communication profits of large bandwidths at high frequencies resulting in high data rates of hundreds of Gbits/s [12]. The provided data rate will enable novel applications of IFE, like cordless virtual reality glasses for video gaming or a live stream of the pilot's view in the cockpit, and bring the IFE to the next level. In addition, high frequencies result in small antenna sizes which minimize the required

Manuscript received 17 February 2022; revised 30 May 2022; accepted 2 July 2022. Date of publication 20 July 2022; date of current version 17 November 2022. This work was supported by the German Research Foundation (DFG) "Meteracom—Metrology for THz Communications" under Grant FOR 2863. *(Corresponding author: Tobias Doeker.)*

The authors are with the Institute for Communications Technology, Technische Universität Braunschweig, 38106 Brunswick, Germany (e-mail: doeker@ifn.ing.tu-bs.de; eckhardt@ifn.ing.tu-bs.de; kuerner@ifn.ing.tu-bs.de).

Color versions of one or more figures in this article are available at https://doi.org/10.1109/TAP.2022.3191218.

Digital Object Identifier 10.1109/TAP.2022.3191218

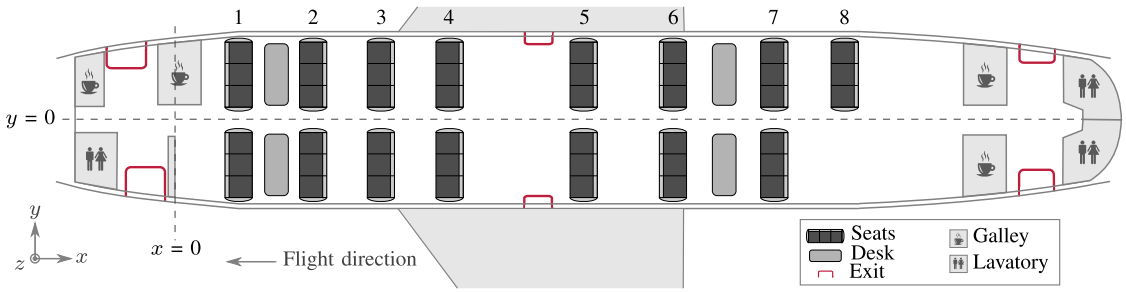

Fig. 1. Layout of the aircraft cabin (Boeing 737-500).

device dimension and the weight of the technical architecture as the antenna size is proportional to the wavelength [13]. On the other hand, the antennas have to be highly directive to cover the high path losses at low THz frequencies which makes radio channel models and their spatial characteristics even more important [14].

Meanwhile, the low THz band is a topic of general interest and a candidate for the next generation of mobile systems [13]. The first THz standard IEEE 802.15.3d on switched point-to-point links was introduced in 2017 [15]. In addition, frequency bands in the range of 275–450 GHz were revealed for the operation of fixed and land mobile service applications at the World Radiocommunication Conference 2019 (WRC-19) [16]. However, impact on other services operating in these frequency bands, such as earth observation satellites, has to be avoided. Therefore, further investigations and sharing studies are needed as measurements have shown a low attenuation of the aircraft cabin windows at 60 GHz [17] and 300 GHz [18].

Recent research activities at 300 GHz examine inter-wagon communications in high speed trains [19], V2X communications [20], wireless backhaul links [21], chip-to-chip communication [22], as well as communication links within data centers [23]. As to the authors knowledge, research activities examining 300 GHz as a candidate for a wireless IFE system have not been reported so far.

To close this gap, the contribution of this article is twofold.

1) A comprehensive measurement campaign examines the main propagation effects in the complex aircraft environment in realistic application scenarios at 300 GHz. The channel properties such as power delay profile (PDP), power angular profile (PAP), path loss (PL), delay spread (DS), and angular spread (AS) are reported and main propagation paths are illustrated.
2) The directional measurement results lay the basis for realistic PL models that allow for an in-depth analysis of the scenarios and enable a comparison of different locations of low THz APs. The model and the measurement data serve as components for further link- and system-level simulations of wireless IFE systems.

The rest of the article is structured as follows. Section II introduces the measurement equipment, the calibration technique, and the key parameters of the radio channel characterization. The ensuing radio channels under investigation are grouped into two parts: communication links and potential interference links. First, in Section III the measurement setups and results for examining the reflections at the seats and the cabin sidewall are presented, complemented by a detailed PL model. Then, potential interference link scenarios between two UEs are investigated in Section IV with a focus on reflections at the passenger service unit (PSU) panel and in the azimuth plane. Finally, the article is summarized and concluded in Section V.

II. Measurement Methodology

To measure and analyze the radio channel, time-domain channel sounding was performed. In this section, the measurement methodology is presented, starting with the introduction of the measurement environment in Section II-A. After that, the channel sounder equipment and its related calibration methodology are described in Sections II-B and II-C, respectively. Finally, the parameters characterizing the radio channel are briefly presented in Section II-D.

A. Measurement Environment

All measurements were conducted in the passenger cabin of a Boeing 737-500 of which the layout is shown in Fig. 1. The passenger cabin has a width of 3.5 m and a total length of 22 m, but the effective length of the cabin in the given airplane was limited to the area between the partition wall in front of the first row and the galley in the rear part of the cabin and had a length of 16.7 m. In the center aisle, the cabin had a height of 2.14 m. It should be noted that this aircraft is out of service and is used as a training center. Therefore, the layout of the cabin differs from a standard aircraft cabin. As can be seen in Fig. 1, there were only eight rows of seats distributed over the whole cabin range. Furthermore, additional desks were installed between row 1 and 2 as well as between row 6 and 7. The seats in row 1 and 6 were oriented inversely to the flight direction. All rows were equipped with six standard seats with a backrest height of 1.15 m, a width of approximately 0.5 m, and a depth of approximately 0.6 m, positioned on the left and right side with three seats each. The center aisle between the seats had a width of approximately 0.45 m. Above the seats, overhead stowage compartments were installed, which reduced the standard height of the cabin to approximately 1.6 m. The overhead stowage compartments were extended over the whole length of the passenger cabin and included the PSU panels which provide, among others, reading lights, personal air conditioning, and oxygen masks. In the center

TABLE I
TECHNICAL PARAMETERS OF THE CHANNEL SOUNDER [24]

Parameter	Value
Clock frequency	9.22 GHz
Bandwidth	8 GHz
Chip duration	108.5 ps
M-sequence order	12
Sequence length	4095
Sequence duration	444.14 ns
Subsampling factor	128
Acquisition time for one CIR	56.9 µs
Measurement rate	17 590 CIR/s
Center frequency	304.2 GHz

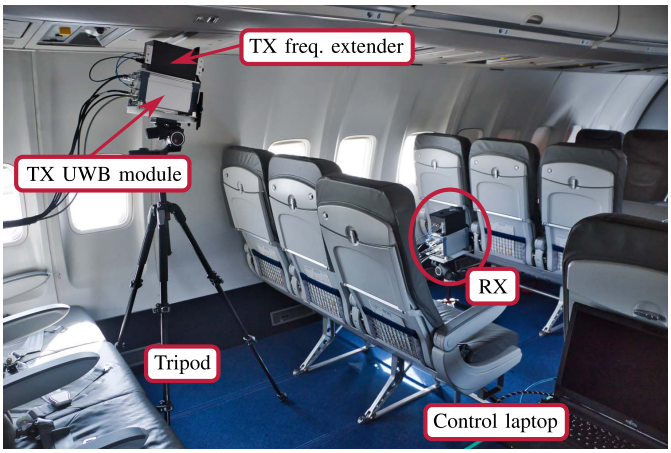

Fig. 2. Partial illustration of the general measurement setup.

aisle, the overhead stowage compartments had a distance of 1 m between the right and left-hand sides.

For all measurements, the origin of the coordinate system was placed in the front of the passenger cabin for the x-direction and in the middle of the cabin for the y-direction. The zero reference in z-direction was placed on the cabin floor. The origin and the corresponding coordinate system are also shown in Fig. 1.

B. Measurement Equipment

In all measurement setups, a sub-mmWave channel sounder was used to measure the channel impulse response (CIR). To do so, the channel sounder transmits a pseudorandom noise (PN) sequence with a bandwidth of approximately 8 GHz at a center frequency of 304.2 GHz. The CIR is calculated by cyclic correlation of the transmitted and received signal. The important key parameters of the channel sounder are summarized in Table I.

To reach the center frequency of 304.2 GHz, a UWB signal in the range from 5.2 to 13.2 GHz is upconverted using frequency extenders. Fig. 2 gives a partial illustration of the general measurement setup and Fig. 3 shows a schematic block diagram of the channel sounder and its main components. The base unit provides the power and the clock signal at 9.22 GHz for the UWB modules. By means of the base clock, the PN

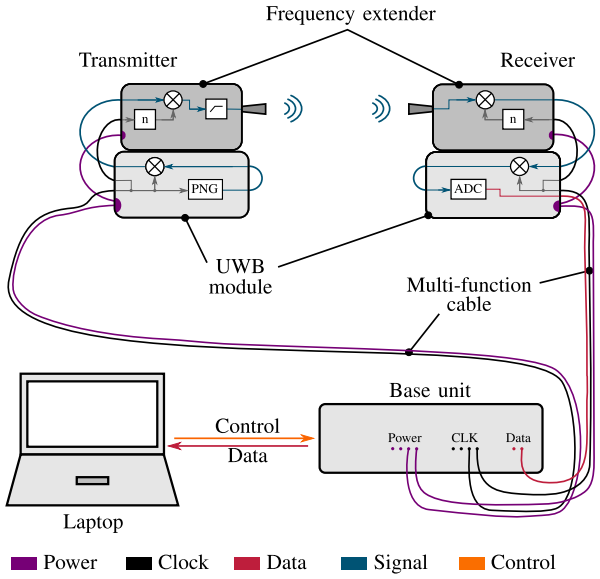

Fig. 3. Schematic block diagram of the channel sounder.

sequence with a length of 4095 chips and a chip duration of 108.5 ps is generated by the PN sequence generator (PNG) and subsequently upconverted into the range of the UWB by the TX UWB module. Within the TX frequency extender, the UWB signal is upconverted into the low THz band using a multiple of the base clock and radiated with a transmit power of −23.7 dBm. The same approach is followed to downconvert the received signal by a multiple of the base clock.

For all measurements, standard gain horn antennas with a gain of $G_{\mathrm{TX,dB}} = G_{\mathrm{RX,dB}} = 26.4$ dBi and a half power beamwidth (HPBW) of 8.5° were used to transmit and receive the signal. The antennas compensate for the high free space path loss (FSPL) at THz frequencies and act as a spatial filter that allows for a sensing of the multipath components (MPCs) in the spatial domain. After downconversion, the received baseband signal is sampled by analog-to-digital converters (ADCs) with in-phase and quadrature using a subsampling factor of 128. Finally, the data is sent to the control laptop that calculates the cross correlation and obtains the CIR. In this way, 17 590 CIRs can be recorded per second. Further information on the channel sounder can be found in [24].

C. Calibration and Post-Processing

The PNG and the subsampling mechanism in the ADCs introduce an arbitrary delay in the CIR every time the sounder is switched on. To compensate for the delay and the varying transmit power of the individual UWB modules, a calibration based on a back-to-back (B2B) measurement has to be performed. The relative path loss obtained from the B2B measurement is compared to the known attenuation of the wave guides and the calibration factor in terms of attenuation is calculated as described in [18]. Furthermore, the main peak of the B2B measurements marks the known delay of the wave guides and thus makes it possible to deduce a time zero reference τ_0. The delay in the measurement τ_{meas} can

be calibrated referring to the time zero reference

$$\tau = \tau_{\text{meas}} - \tau_0. \tag{1}$$

In order to augment the dynamic range of the channel sounder, various CIRs are averaged in a quasi-static measurement scenario. In total, 8192 measurements and 2048 measurements were averaged resulting in a dynamic range of approximately 80 and 74 dB for the tripod-based and rotation-based scenarios, respectively. However, the spurious free dynamic range of the channel sounder amounts to 20 dB and is independent of the averaging because the spurious peaks are caused by the system itself and are linked to the incident signal power. However, this affects the dynamic range only if a strong component is received. Finally, the data is processed in MATLAB to calculate the channel parameters that are described in the next section.

D. Channel Parameters

Based on the data that is recorded during the channel sounding, the channel is characterized by its following parameters.

1) Channel Impulse Response: A wide-band radio channel is characterized by its complex CIR $\underline{h}_{\text{c}}(t, \tau)$ where the index "c" indicates the channel. The CIR is a function of the time t and the multipath characteristics, described by τ. In the case of a quasi-static channel, the CIR only depends on the multipath characteristics and can be described by [25]

$$\underline{h}_{\text{c}}(\tau) = \sum_{i=1}^{N} \underline{c}_i \cdot \delta(\tau - \tau_i) \tag{2}$$

where N is the number of MPCs, $\underline{c}_i$ is the complex time-independent amplitude of the ith MPC with its delay τ_i, and $\delta(\cdot)$ denotes the Dirac function. As described in Section II-B, the measurements were conducted using highly directive antennas. Therefore, each measurement represents a spatially limited CIR

$$\underline{h}_{\text{c,sect},\varphi_{\text{TX}},\varphi_{\text{RX}},\theta_{\text{TX}},\theta_{\text{RX}}}(\tau) = \sum_{i=1}^{N} \underline{c}_{\text{i}} \cdot \delta(\tau - \tau_i) \tag{3}$$

where φ_{TX} and φ_{RX} denote the azimuth angle of the TX and the RX, respectively, and θ_{TX} and θ_{RX} denote the elevation angle of the TX and the RX, respectively. The index "sect" indicates that it is a spatially limited CIR of the respective sector. In this article, we consider only either azimuth plane or elevation plane. Therefore (3) can be written as

$$\underline{h}_{\text{c,sect},\Lambda_{\text{TX}},\Lambda_{\text{RX}}}(\tau) = \sum_{i=1}^{N} \underline{c}_i \cdot \delta(\tau - \tau_i) \tag{4}$$

with Λ representing either the azimuth or the elevation plane ($\Lambda \in \{\varphi, \theta\}$).

Following [26], a quasi omni-directional CIR (ODCIR) $\underline{\tilde{h}}_{\text{c}}(\tau)$ can be calculated as a superposition of the MPCs of the spatially limited CIRs

$$\left|\underline{\tilde{h}}_{\text{c}}(\tau)\right|^2 = \sum_{\Lambda_{\text{TX}}} \sum_{\Lambda_{\text{RX}}} \sum_{k} \left|\underline{h}_{\text{c,sect},\Lambda_{\text{TX}},\Lambda_{\text{RX}}}(\tau_k)\right|^2 \cdot \delta(\tau - \tau_k) + \sum_{l} \left|\underline{n}(\tau_l)\right|^2 \cdot \delta(\tau - \tau_l) \tag{5}$$

where τ_k denotes the delay of the kth multipath, $\underline{n}(\cdot)$ denotes a synthetically generated noise, and τ_l denotes the delay of the lth sample. The synthetically generated noise $\underline{n}(\cdot)$ contains zero-mean Gaussian distributed complex values, generated based on the standard deviation of the noise of the measurement. It is notable that, here and in the following, k indexes a defined component of the CIR whereas l indexes each sample of the CIR. The defined components of the CIR, indexed by k, are the MPCs of which the amplitude is higher than a defined threshold which is here chosen as 15 dB over the noise floor. In addition, all values 10 dB below the main peak of each spatially limited CIR are discarded due to the spurious peaks and the spreading of the pulse caused by the measurement equipment. A threshold of 10 dB is a good trade-off between the reduction of the imperfection of the measurement equipment and the sensitivity of detecting MPCs.

2) Power Delay Profile: The PDP describes the power which is received by the different MPCs that are separated in time. The PDP is given by the absolute square of the CIR [25]

$$P_\tau(\tau) = \left|\underline{h}_{\text{c}}(\tau)\right|^2 \tag{6}$$

and provides the basis for the calculation of the temporal radio channel characteristics. In this work, the PDP is always based on the ODCIR $\underline{\tilde{h}}_{\text{c}}(\tau)$.

3) Power Angular Profile: Similar to the definition of the PDP, the PAP describes the received power by the different MPCs that are spatially separated and is given by the absolute square of the CIR in the angular domain. In principle, the PAP can be given as a function of φ_{TX}, φ_{RX}, θ_{TX} or θ_{RX}, the angle of departure (AOD) and angle of arrival (AOA) in the azimuth and the elevation plane, respectively. The CIR in the angular domain is, here, also based on the spatially limited CIRs and can be calculated as the summation of the spatially limited CIRs

$$P_\Phi(\Lambda_\alpha) = \sum_{\Lambda_\beta} \sum_{k} \left|\underline{h}_{\text{c,sect},\Lambda_\alpha,\Lambda_\beta}(\tau_k)\right|^2 \tag{7}$$

where α and β denote TX and RX, respectively, or vice versa. The synthetically generated noise is omitted to increase the dynamic range.

Besides the 1-D PAP (7), also a 2-D PAP can be given that describes the received power as a function of the AOD and AOA

$$P_\Phi(\Lambda_{\text{TX}}, \Lambda_{\text{RX}}) = \sum_{k} \left|\underline{h}_{\text{c,sect},\Lambda_{\text{TX}},\Lambda_{\text{RX}}}(\tau_k)\right|^2. \tag{8}$$

4) Delay Spread: The root mean square (rms) DS is defined as the second central moment of the PDP and corresponds to the standard deviation of the mean delay given by [25]

$$\sigma_\tau = \sqrt{\frac{\sum_l \tau_l^2 \cdot P_\tau(\tau_l)}{\sum_l P_\tau(\tau_l)} - \left(\frac{\sum_l \tau_l \cdot P_\tau(\tau_l)}{\sum_l P_\tau(\tau_l)}\right)^2}. \tag{9}$$

For the calculation of the DS all 4095 samples of the ODCIR were considered including the noise.

5) Angular Spread: In line with the DS, the second central moment of the 1-D PAP describes the rms AS. As the PAP is given separately for the AOD and AOA in the elevation and azimuth plane [see (7)], the AS is also given separately for these combinations. However, the angles and the PAP depend on the orientation of the coordinate system which means that the angular spread varies depending on a linear shift of the coordinate system in the angular domain. To avoid this ambiguity, a more suitable definition is given by [27]

$$\sigma_\alpha = \sqrt{\frac{\sum_l |\exp(\mathrm{j}\alpha_l) - \mu_\alpha|^2 \cdot P_\Phi(\alpha_l)}{\sum_l P_\Phi(\alpha_l)}} \tag{10}$$

with

$$\mu_\alpha = \frac{\sum_l \exp(\mathrm{j}\alpha_l) \cdot P_\Phi(\alpha_l)}{\sum_l P_\Phi(\alpha_l)} \tag{11}$$

where α denotes the investigated angular direction, more specifically AOD or AOA in azimuth or elevation plane ($\alpha \in \{\varphi_{\mathrm{TX}}, \varphi_{\mathrm{RX}}, \theta_{\mathrm{TX}}, \theta_{\mathrm{RX}}\}$), and α_l is the angle of the lth component in the PAP.

III. Communication Link

In this section, the radio channel is characterized with regard to a communication link between the AP located at the ceiling and the UE which is used by a seated passenger. All scenarios represent a realistic deployment of TXs and RXs for wireless IFE systems. Since the measurement complexity had to be handled, the setups have to focus on segregated propagation aspects. Here, two effects are analyzed in two different measurement setups: 1) transmission from the TX to the RX by means of reflection at the row of seats in front of the RX and 2) transmission from the TX to the RX by means of the reflection at the cabin sidewall. To realize the desired height, the TX and the RX were always mounted on tripods. Here, only the elevation plane is considered and the rotations were done manually.

All measurements presented in this article are named on the basis of measurement identifications (measIDs) which are organized as follows: All measurements characterize the radio channel with a focus on reflected MPCs. Hence, the measID starts with an "R" for "reflection." The second letter represents the scenario under investigation, "S" for the reflection at the seats and "SW" for the reflection at the sidewall, complemented by an increasing number for each setup. "R-S2," for example, describes the second measurement setup in the first scenario where the reflection at the seats is characterized.

A. Reflection at Seats Scenario

1) Measurement Setup: For all measurements in this scenario, the RX was placed on a tripod between rows 2 and 3 at a height of $d_{\mathrm{height,RX}} = 0.71$ m. The distance between the RX and the seat in front was $d_{\mathrm{RX,anteriorRow}} = 0.30$ m. The TX was placed on a tripod at a height of $d_{\mathrm{height,TX}} = 1.51$ m which is the maximum height that could be realized with the channel sounder below the overhead stowage compartment. The TX and the RX were both placed at the left-hand side of the aircraft (in flight direction) and had the same distance

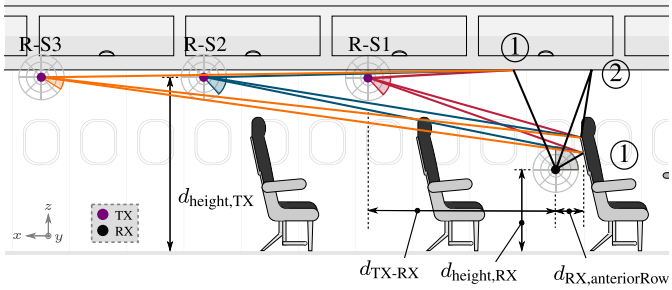

Fig. 4. Measurement setup and selected MPCs of the Reflection at Seats Scenario.

from the cabin wall. The TX was placed at three different x-positions resulting in $d_{\mathrm{TX\text{-}RX}} = \{1.64; 3.08; 4.50\}$ m which corresponds to measID R-S1, R-S2, and R-S3, respectively. It should be noted that the given distances are related to the x-component only. The setup is visualized in Fig. 4.

The AOD and the AOA were varied in the range of $\theta_{\mathrm{TX}} = [90, 138]°$ and $\theta_{\mathrm{RX}} = [2, 90]°$, respectively. However, for R-S3 the range of the AOD was limited to $\theta_{\mathrm{TX}} = [90, 122]°$ because for higher values of θ_{TX} no MPCs were detected. The elevation angles of both, TX and RX, were scanned with a step size of 8° corresponding to the HPBW of the used standard gain horn antennas and matching the state-of-the-art methodology of angular sampled measurements [28]. In this way, the post-processing according to (5) and the calibration process compensate for the impact of the antenna, leading to characteristics of the pure propagation channel. In order to minimize influences of the side lobes, the antennas were used horizontally polarized, thus reducing the side lobes in the vertical plane of interest. Consequently, the measurement results and modeling apply for horizontal polarization only. The TX and the RX were oriented in flight direction, therefore the azimuth angles were $\varphi_{\mathrm{TX}} = \varphi_{\mathrm{RX}} = 180°$. As noted before, only the elevation plane was considered and the azimuth angles were fixed.

2) Results: All measurements show MPCs with a delay lying within a range of 30 ns. This range is shifted by approximately 5 ns between R-S1, R-S2, and R-S3, respectively. The time shift corresponds to the longer time of flight (TOF) due to the longer distance between the TX and the RX. Nevertheless, the shape of the PDPs is always very similar and one dominant propagation path is observed. The measured PDPs based on the ODCIRs are shown in Fig. 5.

Four remarkable MPCs, which are linked and labeled across the different setups in Fig. 5, are identified. The MPCs can be assigned to the following reflection points: The peak ① is a superposition of the MPCs with a reflection of first order at the seat in front of the RX and a reflection of first order at the PSU panel. The peak ② is a reflection of second order at the seat in front of the RX and the PSU panel. The third peak ③ is related to a reflection of first order at the first row of seats, and the fourth peak ④ is related to a reflection of first order at the partition wall in front of the seats at $x = 0$. The rays which correspond to the MPCs ① and ② are illustrated in Fig. 4. The rays are drawn in the scaled schematic considering the

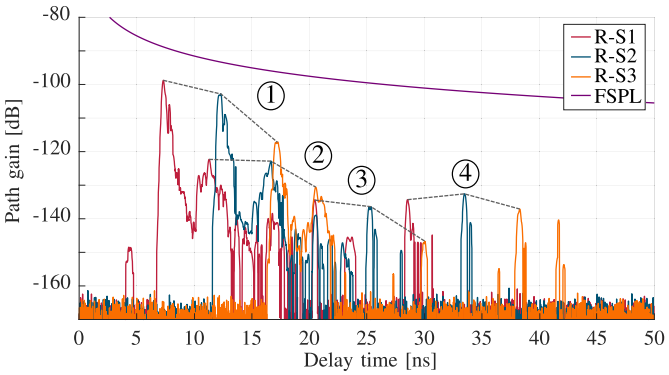

Fig. 5. PDPs of the Reflection at Seats Scenario.

TABLE II
DS AND AS OF THE REFLECTION AT SEATS SCENARIO

measID	DS σ_τ	AS AOD $\sigma_{\theta,\mathrm{TX}}$	AS AOA $\sigma_{\theta,\mathrm{RX}}$
R-S1	0.64 ns	5.2°	13.5°
R-S2	0.84 ns	3.9°	8.4°
R-S3	2.10 ns	4.1°	13.3°

AOD, AOA, and delay time that is translated into a distance. For the sake of clearness and visibility, the rays of the MPCs ③ and ④ are not shown in Fig. 4.

Table II summarizes the DS and the AS for the AOD and the AOA. Due to the fact that the strong first-order reflection ① has to transmit through seats for larger distances between the TX and the RX, the impact of this first MPC decreases with respect to the other MPCs for larger distances $d_{\text{TX-RX}}$ and therefore the DS increases. However, the ratio of the additional losses of the different reflection points and thus the ratio of the received power from the different angles are the same for R-S1 and R-S3. Hence, the AS for those setups is the same. On the other hand, the ratio of the MPC reflected at the seat and the MPC reflected at the PSU panel is higher for R-S2 and therefore the AS is smaller as the impact of the stronger MPC is higher.

To evaluate the reflection loss of the different reflection points, Table III summarizes the covered distances reporting the measured PL, the FSPL based on the delay time of the received MPC [here transferred to a distance of flight (DOF)], and the additional loss, which is calculated as the difference between the FSPL of the DOF and the measured PL. Regarding the reflection at the rear side of the seat in front of the RX—① @ seats—it can be seen that the measurements R-S1 and R-S2 show an additional loss of approximately 10 dB. Besides that, for the same reflection in R-S3 the additional loss is approximately 13 dB higher. With regard to the scenario and as shown in Fig. 4, the signal had to transmit through a row of seats for R-S3. Therefore, it is concluded that the transmission loss of each row of seats is approximately 13 dB. This result is substantiated by the reflections at the seat in row 1 which corresponds to the MPCs ③: here, the signal also had to transmit through one additional row of seats for R-S3 with respect to R-S1 and R-S2 and a difference of approximately 13 dB between the additional losses is observed.

TABLE III
LOSSES OF THE REFLECTION AT SEATS SCENARIO

Reflection point		R-S1	R-S2	R-S3
① @seats	PL	100.34 dB	103.33 dB	119.30 dB
	FSPL	88.82 dB	93.34 dB	96.16 dB
	add. loss	11.52 dB	9.99 dB	23.14 dB
① @PSU	PL	115.61 dB	125.54 dB	139.63 dB
	FSPL	88.91 dB	93.28 dB	96.09 dB
	add. loss	26.70 dB	32.26 dB	43.54 dB
③	PL	134.24 dB	137.06 dB	150.53 dB
	FSPL	97.75 dB	99.56 dB	101.08 dB
	add. loss	36.49 dB	37.50 dB	49.45 dB
④	PL	135.65 dB	134.17 dB	139.32 dB
	FSPL	100.64 dB	102.03 dB	103.16 dB
	add. loss	35.01 dB	32.14 dB	36.16 dB
Theoretical FSPL LOS		87.21 dB	92.04 dB	95.18 dB
Theoretical PL OLOS		-	105.04 dB	108.18 dB
PL of strongest MPC		100.34 dB	103.33 dB	119.30 dB

For the reflection at the PSU panel—① @ PSU—the additional loss differs for all distances. For smaller distances, more power is concentrated to the reflection point at the PSU panel at the corresponding AOD and height of the TX. In addition, the inhomogeneous structure of the PSU panel leads to different reflection losses. It should be noted that the reflection point at the PSU panel was not covered by the measured AOAs and therefore the power was received by the side lobes of the antenna. This fact is considered in the reported values such that the PL compensates for the antenna gain. Finally, the MPCs ④ have the same additional loss in a first order approximation for all three setups because the propagation paths have the same characteristics and identical reflection points.

A further aspect shown in Table III presents the theoretical FSPL of the direct path assuming a LOS scenario and the strongest received MPC, which corresponds to the reflection ① at the rear side of the seat. Due to the seating, there was no LOS between the TX and the RX for R-S2 and R-S3. Here, the direct path will always be blocked by one row of seats, i.e., for these distances we have an obstructed line-of-sight (OLOS) scenario. Therefore, the values for a LOS scenario have to be reduced by the additional loss of one row of seats, i.e., −13 dB. Hence, it appears that the reflection at the seat can serve as an adequate link between the TX and the RX if the LOS is obstructed, for example, by a human body. For R-S1 and R-S3 this alternative link has an additional loss of only 10 dB compared to the direct path and for R-S2 the reflection at the seat has even a lower PL by 2 dB. However, in case of a tall passenger, the path reflected at the front seat could face a significant additional loss, too. Therefore, the path reflected at the PSU panel is a reliable path that is less affected by interfering objects and further evaluated in the following PL model.

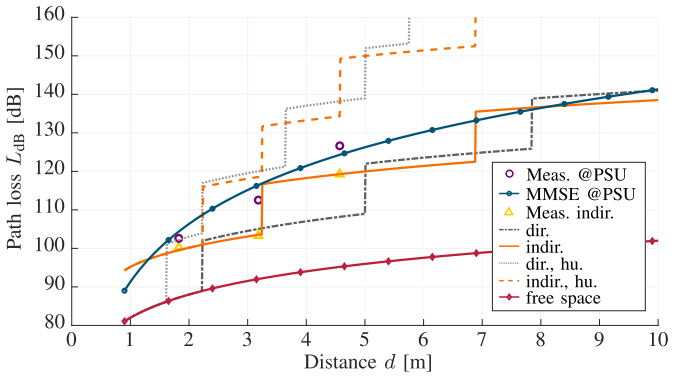

Fig. 6. PL models without and with additional human blockage.

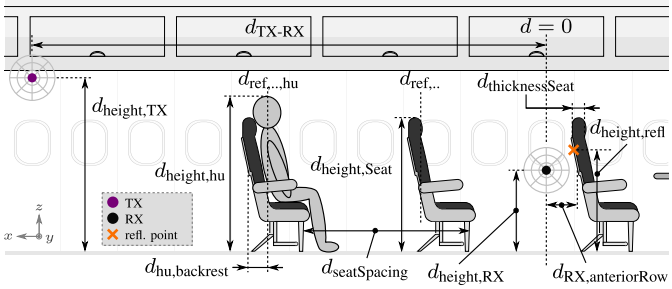

Fig. 7. Schematic illustration as basis for the PL models.

3) PL Model: Based on the measurements, PL models for the examined scenario can be derived as follows.

Starting with the reflection at the PSU panel, the PL model is based on a floating intercept or log-distance PL model given by [25]

$$L_{\text{dB}}(d) = L_{d_0,\text{dB}} + 10\,n\,\log_{10}\left(\frac{d}{d_0}\right) \tag{12}$$

where $L_{d_0,\text{dB}}$ is the PL at a reference distance d_0 (here $d_0 = 1$ m), d describes the distance between the TX and the RX, and n is the PL exponent. Here, d increases with positive x-direction starting at $d = 0$. For the given model, n as well as $L_{d_0,\text{dB}}$ were calculated by minimizing the minimum mean square error (MMSE) between the PL model and the measured values which leads to $L_{d_0,\text{dB}} = 91.3$ dB and $n = 5$. The measurement values as well as the fitted PL model are shown in Fig. 6 as a purple circle and a blue solid line, respectively, where the abscissa describes the distance between the TX and the RX. In terms of the PL model, the RX is kept constant at the position from the measurement setup and the TX is moved backwards on the x-axis (height and distance between the TX and the sidewall are also constant). The FSPL

$$L_{\text{FSPL,dB}}(d) = 20\log_{10}(d) + 20\log_{10}(f) - 147.55\ \text{dB} \tag{13}$$

is added in Fig. 6 as a reference.

A second PL model, emulating the direct path between the TX and the RX, is in general described by a LOS scenario. Nevertheless, due to the seating, the LOS between the TX and the RX is blocked by the seats for an increasing distance. Thus, the PL model for the direct link is given by the FSPL and an additional attenuation of the obstacles

$$L_{\text{dir,dB}}(d) = L_{\text{FSPL,dB}}(d) + \sum_{i=0}^{N} \mathbb{1}_i \cdot L_{\text{seat,trans,dB}} \tag{14}$$

where N is the total number of rows of seats between the TX and the RX at the distance d given by

$$N = \left\lfloor \frac{d_{\text{TX-RX}} + d_{\text{RX,anteriorRow}} + d_{\text{thicknessSeat}}}{d_{\text{seatSpacing}}} \right\rfloor \tag{15}$$

with

$$d_{\text{TX-RX}} = \sqrt{d^2 - (d_{\text{height,TX}} - d_{\text{height,RX}})^2} \tag{16}$$

and $\lfloor\cdot\rfloor$ denoting the floor function. All distances are labeled in Fig. 7. $L_{\text{seat,trans,dB}}$ is the transmission loss of a seat which is given by the measurement results and $\mathbb{1}_i$ is the indicator function which takes 1 if the ith row of seats obstructs the direct link between the TX and the RX and otherwise it takes 0. To evaluate whether a seat obstructs the link, i.e., whether the indicator function is 1 or 0, initially the distance to a reference plane

$$d_{\text{ref,dir},i} = \left(d_{\text{seatSpacing}} - d_{\text{RX,anteriorRow}} - d_{\text{thicknessSeat}}\right) + i \cdot d_{\text{seatSpacing}} \tag{17}$$

is calculated. By means of intercept theorems the height of the ray (representing the propagation path in a ray-optical approach) above the RX at this reference plane can then be calculated as

$$d_{\text{overRX},i} = d_{\text{ref,dir},i} \cdot \frac{d_{\text{height,TX}} - d_{\text{height,RX}}}{d_{\text{TX-RX}}}. \tag{18}$$

Finally, the indicator function can be specified as

$$\mathbb{1}_i = \begin{cases} 1, & \text{if } d_{\text{height,seat}} > d_{\text{height,RX}} + d_{\text{overRX},i} \\ 0, & \text{otherwise.} \end{cases} \tag{19}$$

The PL model is also shown in Fig. 6 as a gray dot-dashed line.

The PL model for the indirect MPC, reflected at the rear side of the seat, is based on the same assumptions. Besides the potential transmission loss of the seats, the additional loss of the reflection at the rear side of the seat has to be considered in this model. The PL model for the indirect link is therefore given by

$$L_{\text{indir,dB}}(d) = L_{\text{FSPL,dB}}(d_{\text{DOF}}) + L_{\text{seat,refl,dB}} + \sum_{i=0}^{N} \mathbb{1}_i \cdot L_{\text{seat,trans,dB}} \tag{20}$$

where d_{DOF} denotes the total distance of the propagation path including the reflection given by

$$d_{\text{DOF}} = \sqrt{\left(d_{\text{height,TX}} - d_{\text{height,refl}}\right)^2 + \left(d_{\text{TX-RX}} + d_{\text{RX,anteriorRow}}\right)^2} + \sqrt{d_{\text{RX,anteriorRow}}^2 + \left(d_{\text{height,refl}} - d_{\text{height,RX}}\right)^2} \tag{21}$$

and $L_{\text{seat,refl,dB}}$ is the reflection loss at the rear side of the seat. $L_{\text{seat,refl,dB}}$ as well as the height of the reflection $d_{\text{height,refl}}$

are given by the measurement results. However, the reference plane for the indicator function is here calculated by

$$d_{\text{ref,indir},i} = (i+1)\cdot d_{\text{seatSpacing}} - d_{\text{thicknessSeat}}. \tag{22}$$

Based on (22), the height of the ray at this reference plane is then given by

$$d_{\text{overRefl},i} = d_{\text{ref,indir},i}\cdot \frac{d_{\text{height,TX}} - d_{\text{height,refl}}}{d_{\text{TX-RX}} - d_{\text{RX,anteriorRow}}} \tag{23}$$

and finally the condition for the indicator function is given by

$$d_{\text{heigth,seat}} > d_{\text{height,refl}} + d_{\text{overRefl},i}. \tag{24}$$

This model is shown in Fig. 6 as a solid, orange line.

Emulating more realistic scenarios, PL models have to account for the additional losses by human blockage in a fully occupied aircraft. In this scenario, the PL can be described by

$$L_{\text{dir,hu,dB}}(d) = L_{\text{dir,dB}}(d) + \sum_{j=0}^{M} \mathbb{1}_j \cdot L_{\text{hu,dB}} \tag{25}$$

and

$$L_{\text{indir,hu,dB}}(d) = L_{\text{indir,dB}}(d) + \sum_{j=0}^{M} \mathbb{1}_j \cdot L_{\text{hu,dB}} \tag{26}$$

where M is the total number of occupied rows of seats, $L_{\text{hu,dB}}$ is the transmission loss of a human body, and $\mathbb{1}_j$ is the indicator function which, here, is 1 if the propagation path is blocked by the human body and 0 otherwise. For this simple model, an average height of 0.82 m for a seated human body referred to the seating surface is assumed, resulting in a height of the human of $d_{\text{height,hu}} = 1.25$ m. The additional loss due to the blockage of a human body amounts to $L_{\text{hu,dB}} = 15$ dB [29]. Furthermore, it is assumed that each row is occupied and therefore

$$M = \left\lfloor \frac{d_{\text{TX-RX}} + d_{\text{RX,anteriorRow}} + d_{\text{hu,backrest}}}{d_{\text{seatSpacing}}} \right\rfloor. \tag{27}$$

The reference plane for the decision whether the indicator function is 1 or 0 is given for the direct link PL model by

$$d_{\text{ref,dir,hu},j} = \left(d_{\text{seatSpacing}} - d_{\text{RX,anteriorRow}} - d_{\text{hu,backrest}}\right) + j\cdot d_{\text{seatSpacing}} \tag{28}$$

and for the indirect link PL model by

$$d_{\text{red,indir,hu},j} = (j+1)\cdot d_{\text{seatSapcing}} - d_{\text{hu,backrest}}. \tag{29}$$

According to (18) and (23), the height of the ray over the RX and over the reflection point can be calculated by

$$d_{\text{overRX,hu},j} = d_{\text{ref,dir,hu},j}\cdot \frac{d_{\text{height,TX}} - d_{\text{height,RX}}}{d_{\text{TX-RX}}} \tag{30}$$

and

$$d_{\text{overRefl,hu},j} = d_{\text{ref,indir,hu},j}\cdot \frac{d_{\text{height,TX}} - d_{\text{height,refl}}}{d_{\text{TX-RX}}}, \tag{31}$$

respectively. Finally, the indicator function is 1 if

$$d_{\text{height,hu}} > d_{\text{height,RX}} + d_{\text{overRX,hu},j} \tag{32}$$

TABLE IV
CONFIGURATION PARAMETERS AND CHOSEN VALUES OF THE PL MODELS

Parameter	Value	Parameter	Value
$L_{d_0,\text{dB}}$	91.3 dB	n	5
d_0	1 m	$L_{\text{seat,trans,dB}}$	13 dB
$d_{\text{RX,anteriorRow}}$	0.30 m	$d_{\text{thicknessSeat}}$	0.10 m
$d_{\text{seatSpacing,given}}$	1.45 m	$d_{\text{seatSpacing,min}}$	0.66 m
$d_{\text{height,TX}}$	1.51 m	$d_{\text{height,RX}}$	0.71 m
$d_{\text{height,seat}}$	1.12 m	$d_{\text{height,refl}}$	0.86 m
$L_{\text{seat,refl,dB}}$	10 dB	$L_{\text{hu,dB}}$	15 dB
$d_{\text{hu,backrest}}$	0.2 m	$d_{\text{height,hu}}$	1.25 m

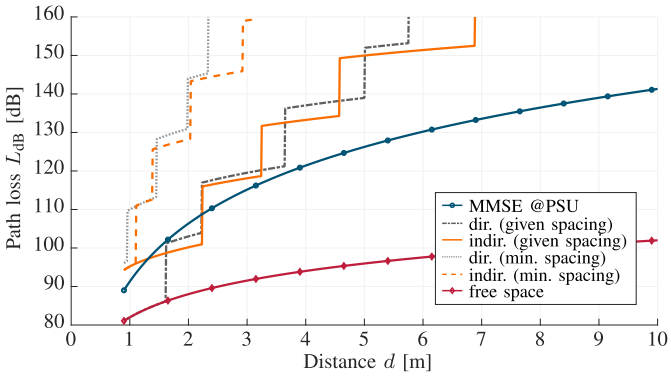

Fig. 8. PL models with human blockage for different seat spacing.

for the direct link PL model and if

$$d_{\text{height,hu}} > d_{\text{height,refl}} + d_{\text{overRefl,hu},j} \tag{33}$$

for the indirect link PL model. Both models are also plotted in Fig. 6. The values of the parameters of the presented PL models are summarized in Table IV.

The different PL models show that the dominant propagation path is a function of the distance between the TX and the RX. If human blockage is not taken into account, either the direct or the indirect link offers the lowest attenuation. This is due to the fact that the indirect link offers good propagation conditions in case the direct link is blocked by the seats. However, if the distance is increased, the indirect link is also blocked by the seats. In that case and for small distances, the direct link has the lower attenuation because the indirect link suffers from additional reflection loss at the seats. For distances >8 m, the PL model constitutes comparable attenuation values for the reflection at the PSU panel with respect to the other propagation paths. It can be assumed that for larger distances this path has the lowest attenuation. If human blockage is considered, the advantage of the propagation path by means of reflection at the PSU panel that is not obstructed by any seat or human is already given for distances >2.5 m.

To emphasize the benefit of the reflection at the PSU panel, the PL models including human blockage are given for different distances between the rows of seats in Fig. 8. As mentioned before, the seating layout in the given airplane was adapted such that the distance between the rows is relatively large

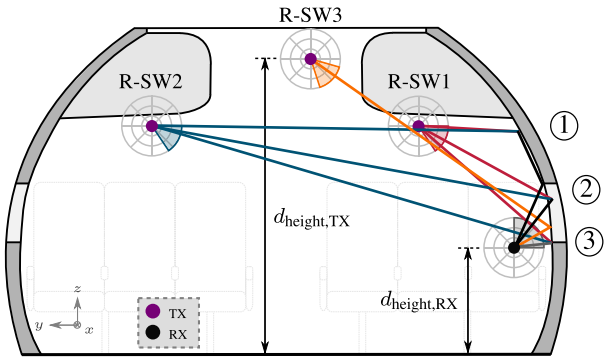

Fig. 9. Measurement setup and selected MPCs for the Reflection at Sidewall Scenario.

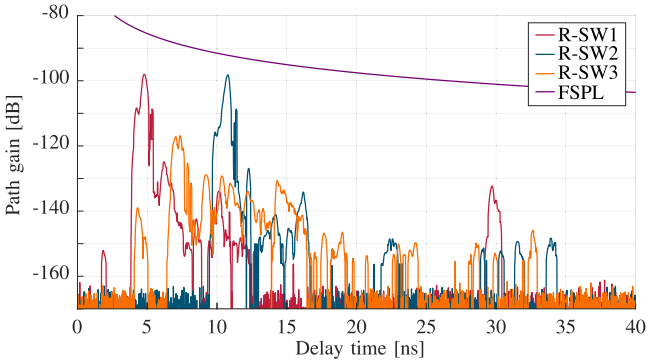

Fig. 10. PDPs of the Reflection at Sidewall Scenario.

(named "given spacing" in Fig. 8). Therefore, the PL models in Fig. 8 with smaller distances (named "min. spacing") between the rows of seats represent more realistic values. For lower seat spacing, the PL for the direct and indirect link increases more significantly and a UE could receive the highest power via the reflection at the PSU panel. Taking advantage of this MPC, the propagation could be improved and steered, for example, by integrating smart reflecting materials and structures in the PSU panel in order to build the foundation for a reliable wireless IFE system.

B. Reflection at Sidewall Scenario

1) Measurement Setup: For all measurements, the TX and the RX were oriented toward the side wall. Therefore, in this case the azimuth angles were set to $\varphi_{\text{TX}} = \varphi_{\text{RX}} = 270°$. In x-direction the TX and the RX were placed at the same position behind the second row of seats. The position of the RX was fixed whereas the TX was placed at three different positions with respect to the sidewall: 1) on the same side of the cabin as the RX (R-SW1); 2) the opposite side (R-SW2); and finally 3) in the middle of the aircraft cabin (R-SW3) with respect to the y-position. For R-SW1 and R-SW2, the TX was positioned at the maximum height below the overhead stowage compartment $d_{\text{height,TX}} = 1.52$ m. For R-SW3, the TX was moved to the maximum possible height below the cabin ceiling $d_{\text{height,TX}} = 1.97$ m. The RX was always at the height of $d_{\text{height,RX}} = 0.71$ m in this scenario, which is visualized in Fig. 9.

TABLE V
DS AND AS OF THE REFLECTION AT SIDEWALL SCENARIO

measID	DS σ_τ	AS AOD $\sigma_{\theta,\text{TX}}$	AS AOA $\sigma_{\theta,\text{RX}}$
R-SW1	0.54 ns	11.1°	15.4°
R-SW2	0.27 ns	4.6°	13.0°
R-SW3	1.98 ns	7.7°	22.9°

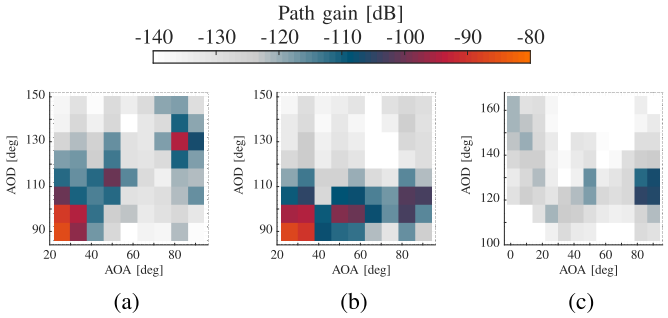

Fig. 11. PAPs of the Reflection at Sidewall Scenario. (a) R-SW1. (b) R-SW2. (c) R-SW3.

Equally to the setup before, the TX and the RX were mounted on tripods. For R-SW1 and R-SW2, the elevation angles of the TX and the RX were scanned in the range of $\theta_{\text{TX}} = [90, 146]°$ and $\theta_{\text{RX}} = [26, 90]°$, respectively, both with a step size of 8°. Given the different height, the elevation angle of the TX was scanned in the range of $\theta_{\text{TX}} = [106, 162]°$ and the elevation angle of the RX in the range of $\theta_{\text{RX}} = [2, 90]°$ for R-SW3. In this scenario the antennas were also mounted in horizontal polarization to reduce the impact of the side lobes.

2) Results: The PDPs of the ODCIR, shown in Fig. 10, have the same characteristics for both TX positions under the overhead stowage compartment (R-SW1 and R-SW2). The timeshift of approximately 5 ns corresponds to the delay due to the larger distance between the TX and the RX in R-SW2. However, the expected additional attenuation for R-SW2 does not occur. In contrast, the PDP shows much weaker MPCs when the TX is placed under the ceiling (R-SW3) because the signal is obstructed by the overhead stowage compartment. On one hand, this leads to less multipath propagation, but on the other hand, the LOS of the seat at the window could be blocked.

Table V summarizes the DS and AS. For R-SW1 and R-SW2, the DS is in the same order of magnitude. The deviation of 0.2 ns is caused by the strong MPC in R-SW1 at 30 ns. Without this MPC, R-SW1 and R-SW2 would have the same DS due to the identical envelope of the main contribution. The AS of the AOA is also in the same order of magnitude for the measurements R-SW1 and R-SW2 due to the fact that the incident angles of the received signal correspond to the same reflection points. Nevertheless, from the point of view of the TX these reflection points are bundled in a smaller angular range for larger distances and therefore the angular spread of the AOD decreases with larger distance. This fact is also visible in the PAPs shown in Fig. 11. Three strong

TABLE VI
LOSSES OF THE REFLECTION AT SIDEWALL SCENARIO

Reflection points		R-SW1	R-SW2	R-SW3
①	PL	99.73 dB	99.73 dB	-
	FSPL	85.22 dB	92.21 dB	-
	add. loss	14.51 dB	7.52 dB	-
②	PL	112.82 dB	112.50 dB	-
	FSPL	84.74 dB	92.03 dB	-
	add. loss	28.08 dB	20.47 dB	-
③	PL	108.76 dB	119.04 dB	144.88 dB
	FSPL	84.05 dB	91.64 dB	88.93 dB
	add. loss	24.71 dB	24.43 dB	55.95 dB

MPCs can be identified which correspond to the reflection points shown in Fig. 9. ① is a reflection of second order with a first reflection at the fuselage and a second reflection at the fuselage and window, respectively. Besides that, ② and ③ are first-order reflections at the window and fuselage, respectively. Due to the similar delay time of these reflections, the main contribution in the PDPs is a superposition of these MPCs.

The reflection loss that corresponds to the additional PL of the measurement with respect to the theoretical FSPL based on the DOF is summarized in Table VI. First, it is notable that the reflection loss for reflection ① is lower than for reflection ② and ③, even though ① is a reflection of second order. It is assumed that for ① the signal was reflected mainly at the metallic fuselage that may add a collimating effect because of its curvature, unlike for ② and ③, where the signal was reflected at the window which leads to a significantly higher loss. Furthermore, the reflection loss for R-SW1 is approximately 7 dB higher compared to R-SW2 for ① and ②. Hence, the reflection losses differ for the different setups. It can be assumed that for R-SW2 the wave was both times reflected at the fuselage for ①, in contrast to R-SW1, where the second reflection occurred at the window with a higher reflection loss than the fuselage. The same holds for ② where the wave for R-SW1 was reflected at the window whereas it was reflected at the fuselage in R-SW2. Nevertheless, due to the angular resolution and HPBW the reflections are associated with the same AOA. R-SW3 was also reflected at the window so the value is comparable to ③ for R-SW1 and R-SW2, but due to the blockage by the overhead stowage compartment the additional loss is significantly higher in this case.

In conclusion, the measurements of the reflections at the sidewall show that the fuselage has a significant impact on the wave propagation and acts like a collimating reflector with a reflection loss of approximately 7 dB. The reflections at the fuselage have to be considered for communication link simulations either as a useful MPC or as an interfering MPC that might cause inter-symbol interference (ISI). Moreover, a single THz AP can cover the left and right row of seats from the channel's perspective. In contrast, an AP mounted underneath the ceiling in the main aisle has the disadvantage of the obstruction of the LOS path due to the blockage by the overhead stowage compartments.

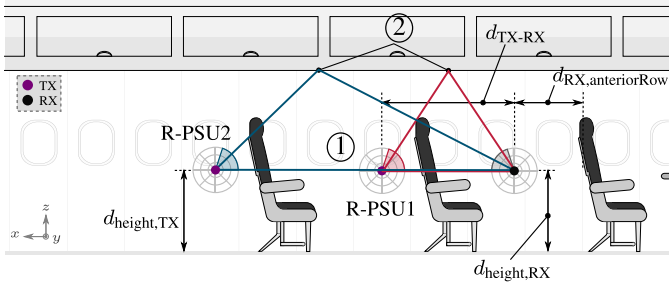

Fig. 12. Measurement setup and selected MPCs of the Reflection at PSU Panel Scenario.

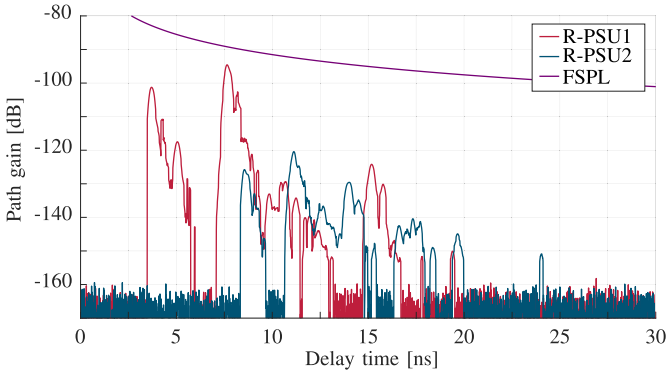

Fig. 13. PDPs of the Reflection at PSU Panel Scenario.

IV. INTERFERENCE LINK

Unlike the previous section, here the radio channel is characterized regarding interference between two UEs, both located in a realistic position as if used by a seated passenger. In doing so, reflections at the PSU panel (indicated as "PSU" in the measID) and the channel in the azimuth plane (indicated as "AP" in the measID) are examined.

A. Reflection at PSU Panel Scenario

1) Measurement Setup: In this scenario, the TX and the RX both were positioned on tripods at a height of $d_{\text{height,TX}} = d_{\text{height,RX}} = 0.71$ m. The antenna of the TX was oriented in flight direction ($\varphi_{\text{TX}} = 180°$) whereas the RX antenna pointed in the opposite direction ($\varphi_{\text{RX}} = 0°$). Here, only the elevation plane is considered and thus both antennas were horizontally polarized to minimize the impact of the side lobes. The elevation angles of both were scanned in the range of $\theta_{\text{TX}} = \theta_{\text{RX}} = [18, 90]°$ with an increment of 8°. The RX was placed between row 2 and 3. The distance between the row of seats in front of the RX and the RX itself was $d_{\text{RX,anteriorRow}} = 0.55$ m. In R-PSU1 the TX was placed in the adjacent row with $d_{\text{TX-RX}} = 1.16$ m and in R-PSU2 with one row in between with $d_{\text{TX-RX}} = 2.61$ m in x-direction. In y-direction the TX and the RX both had the same distance to the cabin side wall. A schematic view of the scenario is shown in Fig. 12.

2) Results: In this scenario, the PDPs, based on the ODCIRs and plotted in Fig. 13, have a very similar shape and two main peaks are identified. The peaks correspond to the OLOS

TABLE VII
DS AND AS OF THE REFLECTION AT PSU PANEL SCENARIO

measID	DS σ_τ	AS AOD $\sigma_{\theta,\mathrm{TX}}$	AS AOA $\sigma_{\theta,\mathrm{RX}}$
R-PSU1	1.47 ns	16.7°	16.3°
R-PSU2	1.70 ns	18.9°	11.8°

TABLE VIII
LOSSES OF THE REFLECTION AT PSU PANEL SCENARIO

Reflection point		R-PSU1	R-PSU2
①	PL	101.68 dB	126.50 dB
	FSPL	82.87 dB	90.15 dB
	add. loss	18.81 dB	36.35 dB
②	PL	98.10 dB	122.95 dB
	FSPL	89.28 dB	92.45 dB
	add. loss	8.82 dB	30.50 dB

path through the seats and a first-order reflection at the PSU panel, as visualized via rays in Fig. 12. It can be observed that the difference of the delay time between the two main peaks becomes smaller if the distance between the TX and the RX is increased. Hence, the larger the distance between the TX and the RX, the smaller the difference between the path length of the OLOS path and the path reflected at the PSU panel. Nevertheless, the DS increases because the amplitudes of the MPCs approach each other. Table VII summarizes the DS and the AS. Regarding the AS, R-PSU1 has the same AS for the AOD and the AOA because the point of reflection was almost in the center between the TX and the RX related to the x-direction. For R-PSU2, the point of reflection at the PSU panel was closer to the TX and therefore the AS of the AOD is higher and the AS of the AOA is smaller compared to R-PSU1.

The additional losses, which again can be computed as the difference between the FSPL based on the DOF and the measured PL, are summarized in Table VIII. For the direct path in R-PSU1 an additional loss of 18.81 dB is calculated. The larger distance and two seats between the TX and the RX lead to an additional loss of 36.35 dB for R-PSU2. Therefore, the additional loss of a row of seats in this scenario can be given by approximately 18 dB. This contrasts the results in Section III-A2 where 13 dB is given as the additional loss of one seat. However, for the calculated additional loss in Section III-A2 a wave transmitting through the headrest is considered. Here, the signal transmits through the backrest which also includes the collapsible table. This leads to a higher attenuation of 5 dB compared to the transmission loss of the headrest. On the other hand, Table VIII shows that the reflection loss at the PSU panel is smaller than the transmission loss through the seats. Regarding the interference channel, the reflection at the PSU panel is more important than the direct path and could lead to strong interference. More specifically, the path ② constitutes a significant interfering component if an AP is integrated in the PSU panel at the point of reflection in R-PSU and several UEs have an active transmission.

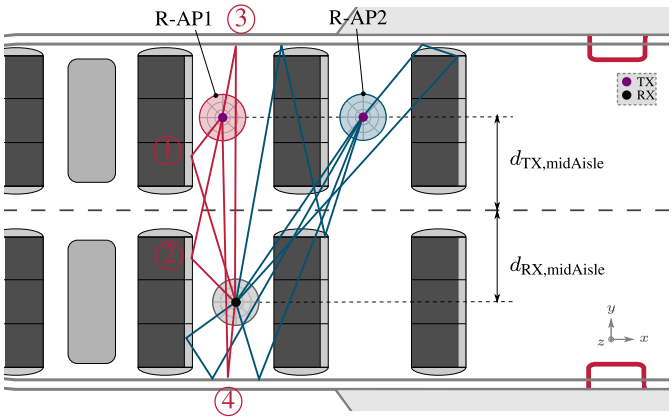

Fig. 14. Measurement setup and selected MPCs of the Reflection in Azimuth Plane Scenario.

Even directional antennas will not filter this MPC since they are aligned toward the AP. Consequently, interference mitigation, for example, by frequency multiplexing, has to be considered in the system design.

B. Reflection in Azimuth Plane Scenario

1) Measurement Setup: In this setup, the TX and the RX were placed on rotational units which allow an automatic mechanical steering of the antennas in the azimuth plane. Consequently, the TX and the RX were fixed at the elevation angles of $\theta_{\mathrm{TX}} = \theta_{\mathrm{RX}} = 90°$ whereas the azimuth angles were scanned to perform a full rotation, $\varphi_{\mathrm{TX}} = \varphi_{\mathrm{RX}} = [0, 360)°$. To reduce the impact of the sidelobes of the antenna, the polarization of the antenna was changed to vertical polarization. Therefore, the measurement results apply to vertical polarization only. The step size of 8° stayed constant.

The mounting of the TX and the RX onto the rotational units resulted in a height of $d_{\mathrm{height,TX}} = d_{\mathrm{height,RX}} = 0.77$ m which is comparable to the height of the UE in previous scenarios and still emulates a typical height of a UE held in the hand of a seated passenger. Both, TX and RX, had the same distance to the middle aisle with respect to the y-coordinate and therefore also to the cabin sidewall of $d_{\mathrm{TX,midAisle}} = d_{\mathrm{RX,midAisle}} = 0.97$ m but were placed at different sides of the airplane. In this scenario, the RX was always fixed whereas the TX was positioned in two different rows: First, both were positioned between row 2 and 3 (R-AP1) followed by the TX placed between row 3 and 4 (R-AP2). This results in a direct path distance between the TX and the RX of $d_{\mathrm{TX\text{-}RX}} = \{1.95, 2.36\}$ m. The setup is shown in a schematic top view in Fig. 14.

2) Results: The PDPs (see Fig. 15) as well as the PAPs (see Fig. 16) indicate a rich multipath environment with respect to the azimuth plane. For R-AP1, the LOS component dominates the PDP which leads to a small DS of $\sigma_{\tau,\mathrm{R\text{-}AP1}} = 0.90$ ns. If the LOS path is obstructed, as given in R-AP2, the reflected MPCs still have quite similar amplitudes which in this case increase the DS up to $\sigma_{\tau,\mathrm{R\text{-}AP2}} = 3.69$ ns. The same behavior can be observed for the AS summarized in Table IX which is much smaller for R-AP1 compared to R-AP2 due to the strong LOS

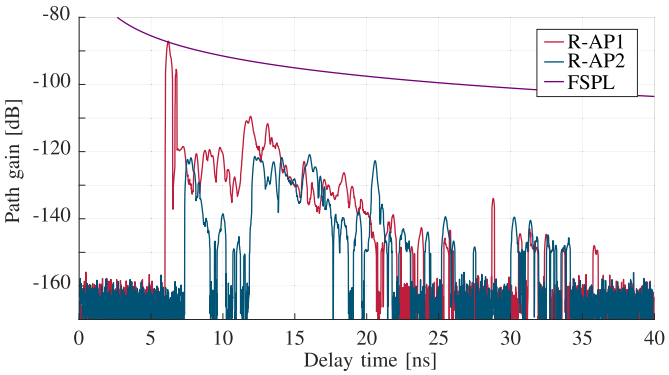

Fig. 15. PDPs of the Reflection in Azimuth Plane Scenario.

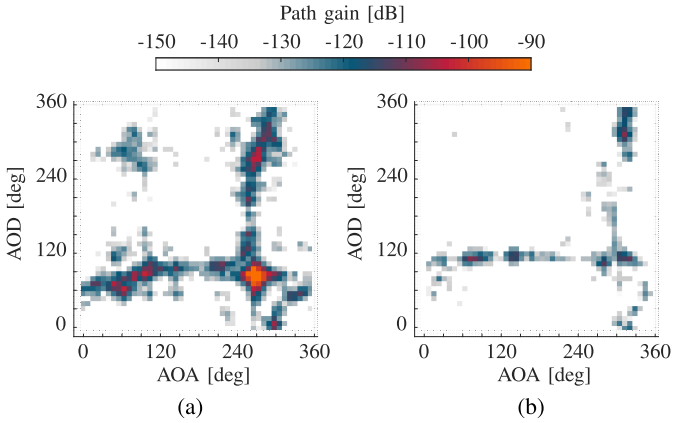

Fig. 16. PAPs of the Reflection in Azimuth Plane Scenario. (a) R-AP1. (b) R-AP2.

component in R-AP1. In Fig. 14, selected MPCs are illustrated where the MPCs shown for R-AP2 give an impression of the reflections creating the rich multipath environment.

For R-AP1, another effect in the azimuth plane is indicated with the selected MPCs shown in Fig. 14: The MPCs are distributed symmetrically. MPC ① is a first-order reflection at the row of seats in front of the TX. Symmetrically, the MPC ② is the first-order reflection at the row of seats in front of the RX. Same holds true, for example, for the MPCs ③ and ④ caused by the first-order reflection at the cabin sidewall. This is also emphasized by the ASs which have similar values for the AOD and AOA. Furthermore, the PAPs show a typical and symmetric cross shaped distribution of the MPCs over the azimuth plane. Comparable results and distributions of MPCs are also observed in data centers [30] and trains [31]. However, long aisles are investigated in these scenarios but it can be seen that in all scenarios the geometry of canyon-like environments leads to comparable characteristics of the channel. Due to the rich multipath constellation especially in the same row where the path is not blocked by seats, the interference of other UEs by means of the reflection in the azimuth plane cannot be neglected.

Regarding the additional losses in the azimuth plane, which are summarized in Table X, the reflection at the backrest of the seats—reflection ① and ②—has higher additional losses compared to the reflection losses in Section III-A as we observe a rather non-specular reflection. With respect to the reflection at the fuselage—reflection ③ and ④—the additional losses are equal to reflection ③ in Section III-B.

TABLE IX
DS AND AS OF THE REFLECTION IN AZIMUTH PLANE SCENARIO

measID	DS σ_τ	AS AOD $\sigma_{\varphi,\mathrm{TX}}$	AS AOA $\sigma_{\varphi,\mathrm{RX}}$
R-AP1	0.90 ns	11.8°	12.6°
R-AP2	3.69 ns	53.3°	52.3°

TABLE X
LOSSES OF THE REFLECTION IN AZIMUTH PLANE SCENARIO (R-AP1)

Reflection point	①	②	③	④
PL	126.91 dB	124.58 dB	115.95 dB	115.96 dB
FSPL	88.22 dB	88.71 dB	93.04 dB	92.84 dB
add. loss	38.69 dB	35.87 dB	22.91 dB	23.12 dB

V. CONCLUSION

Tackling the challenge of a high density of passengers in an aircraft cabin, low THz communications has the potential to serve high data rates for all passengers with only a few APs. To get a better understanding of the radio channel characteristics, we presented measurements at 300 GHz within an aircraft cabin. In four different setups, we examined the behavior of the low THz radio channel with regard to a communication link between the AP and the UE as well as an interference link between two UEs. Since the space and the number of APs are limited within the aircraft, it is challenging to establish a LOS communication between the AP and all UEs. Hence, we designed our measurement setups such that they emulate realistic application scenarios and investigated especially reflections in the aircraft cabin in order to capture the complex propagation environment.

The measurements show that in general the radio channel at low THz frequencies within an aircraft is characterized by complex and rich multipath propagation which, on the one hand, could enhance the communication link, but on the other hand, could also lead to strong interference.

The communication link scenarios illustrate that various MPCs contribute to the PDP. Channel characteristics like the additional PL, the DS, and the AS are reported and explained. The measurements reveal a reflection loss of the seats of 10 dB. The transmission loss of seats amounts to 13 and 18 dB in the region of the headrest and at the height of the collapsible table, respectively. A similar PL of a reflected path is measured regardless of whether the AP is placed at the same or the opposite side of the aircraft, following that one TX can serve for a whole row of seats. In contrast, a high additional loss due to the overhead stowage compartment occurs if the TX is placed at the ceiling of the middle aisle.

The interference setups reveal a low reflection loss at the PSU panel that could lead to strong interference between two UEs that communicate with the same AP. Also, the rich

multipath propagation in the horizontal plane at the typical height of a UE suggests potential interference between both sides of the aircraft, especially in the same row.

A deterministic and geometry-based channel model demonstrates the impact of the various MPCs and their dependency on the distance between the TX and the RX. Modeled with FSPL and additional reflection and blockage losses extracted from measurements, the impact from the environment, for example, seat spacing and human blockage, on the channel is demonstrated. The model suggests that the reflection at the PSU panel is an appropriate propagation path for a reliable communication over several rows of seats, especially if human blockage is considered. Combined with smart reflecting surfaces, the overhead stowage compartment represents a promising location for a low THz AP.

Further propagation and link-level simulations considering the influence of beam-steerable antennas will investigate the interference on the system performance. In this way, the reported measurements and the channel model contribute to the design of future wireless IFE systems at low THz frequencies.

ACKNOWLEDGMENT

The authors would like to thank the Lufthansa Technical Training GmbH (LTT), Hamburg, Germany, for providing the aircraft. In particular, they would like to thank Mike Stehr and Dirk Akra, staff members at LTT, for their support during the measurements.

REFERENCES

[1] Cisco, *Cisco Annual Internet Report (2018–2023)*, Cisco Systems, San Jose, CA, USA, 2020. [Online]. Available: https://www.cisco.com/c/en/us/solutions/collateral/executive-perspectives/annual-internet-report/white-paper-c11-741490.pdf

[2] S. Scott-Hayward and E. Garcia-Palacios, "Delivering HD video for wireless in-flight entertainment with IEEE 802.15.3c," in *Proc. IET Irish Signals Syst. Conf. (ISSC)*, Maynooth, Ireland, 2012, pp. 1–6.

[3] D. Folden *et al.*, "An aircraft cabin wireless system for games and video entertainment," *ACM Comput. Entertainment*, vol. 5, no. 1, pp. 7–24, 2007.

[4] L. Schuessele, T. Felhauer, A. Christ, T. Klausmann, A. Kaufmann, and A. Gerold, "A novel broadband communication system for aircraft in-flight entertainment applications," in *Proc. IEEE Int. Symp. Broadband Multimedia Syst. Broadcast. (BMSB)*, Nuremberg, Germany, Jun. 2011, pp. 1–6.

[5] N. R. Diaz and J. E. J. Esquitino, "Wideband channel characterization for wireless communications inside a short haul aircraft," in *Proc. IEEE 59th Veh. Technol. Conf. (VTC Spring)*, Milan, Italy, May 2004, pp. 223–228.

[6] J. Jemai *et al.*, "UWB channel modeling within an aircraft cabin," in *Proc. IEEE Int. Conf. Ultra-Wideband*, Hannover, Germany, Sep. 2008, pp. 5–8.

[7] S. Chiu, J. Chuang, and D. G. Michelson, "Characterization of UWB channel impulse responses within the passenger cabin of a Boeing 737–200 aircraft," *IEEE Trans. Antennas Propag.*, vol. 58, no. 3, pp. 935–945, Mar. 2010.

[8] M. Peter and W. Keusgen, "A component-based time domain wideband channel sounder and measurement results for the 60 GHz in-cabin radio channel," in *Proc. 2nd Eur. Conf. Antennas Propag. (EuCAP)*, Edinburgh, U.K., 2007, pp. 1–6.

[9] A. Garcia, W. Kotterman, U. Trautwein, D. Brückner, J. Kunisch, and R. Thomä, "60 GHz time-variant shadowing characterization within an Airbus 340," in *Proc. 4th Eur. Conf. Antennas Propag. (EuCAP)*, Barcelona, Spain, Apr. 2010, pp. 1–5.

[10] C. Quintana, V. Guerra, J. Rufo, J. Rabadan, and R. Perez-Jimenez, "Reading lamp-based visible light communication system for in-flight entertainment," *IEEE Trans. Consum. Electron.*, vol. 59, no. 1, pp. 31–37, Feb. 2013.

[11] J. Luo, W. Keusgen, A. Kortke, and M. Peter, "A design concept for a 60 GHz wireless in-flight entertainment system," in *Proc. IEEE 68th Veh. Technol. Conf.*, Calgary, AB, Canada, Sep. 2008, pp. 1–5.

[12] I. F. Akyildiz, J. M. Jornet, and C. Han, "Terahertz band: Next frontier for wireless communications," *Phys. Commun.*, vol. 12, pp. 16–32, Sep. 2014.

[13] M. Latva-aho and K. Leppänen, "Key drivers and research challenges for 6G ubiquitous wireless intelligence," 6G Flagship, Univ. Oulu, Oulu, Finland, Tech. Rep. 1, Sep. 2019. [Online]. Available: http://jultika.oulu.fi/files/isbn9789526223544.pdf

[14] I. F. Akyildiz, C. Han, and S. Nie, "Combating the distance problem in the millimeter wave and terahertz frequency bands," *IEEE Commun. Mag.*, vol. 56, no. 6, pp. 102–108, Jun. 2018.

[15] V. Petrov, T. Kurner, and I. Hosako, "IEEE 802.15.3d: First standardization efforts for sub-terahertz band communications toward 6G," *IEEE Commun. Mag.*, vol. 58, no. 11, pp. 28–33, Nov. 2020.

[16] International Telecommunication Union—Radiocommunication Sector, *World Radiocommunication Conference 2019 (WRC-19)—Final Acts*, ITU Publications, Geneva, Switzerland, Mar. 2020.

[17] F. Schwartau, C. Monka, M. Krueckemeier, and J. Schoebel, "Aircraft window attenuation measurements at 60 GHz for wireless in-cabin communication," in *Proc. 11th German Microw. Conf. (GeMiC)*, Freiburg, Germany, Mar. 2018, pp. 319–322.

[18] J. M. Eckhardt, T. Doeker, and T. Kürner, "Indoor-to-outdoor path loss measurements in an aircraft for terahertz communications," in *Proc. IEEE Veh. Technol. Conf. (VTC-Spring)*, Antwerp, Belgium, May 2020, pp. 1–5.

[19] K. Guan *et al.*, "Channel characterization for intra-wagon communication at 60 and 300 GHz bands," *IEEE Trans. Veh. Technol.*, vol. 68, no. 6, pp. 5193–5207, Jun. 2019.

[20] J. M. Eckhardt, V. Petrov, D. Moltchanov, Y. Koucheryavy, and T. Kurner, "Channel measurements and modeling for low-terahertz band vehicular communications," *IEEE J. Sel. Areas Commun.*, vol. 39, no. 6, pp. 1590–1603, Jun. 2021.

[21] J. Edstam, J. Hansryd, S. Carpenter, T. Emanuelsson, Y. Li, and H. Zirath, "Microwave backhaul evolution—Reaching beyond 100 GHz," *Ericsson Technol. Rev.*, vol. 95, pp. 24–37, Feb. 2017.

[22] J. Fu, P. Juyal, and A. Zajic, "Modeling of 300 GHz chip-to-chip wireless channels in metal enclosures," *IEEE Trans. Wireless Commun.*, vol. 19, no. 5, pp. 3214–3227, May 2020.

[23] C. Cheng, S. Sangodoyin, and A. Zajic, "THz cluster-based modeling and propagation characterization in a data center environment," *IEEE Access*, vol. 8, pp. 56544–56558, 2020.

[24] S. Rey, J. M. Eckhardt, B. Peng, K. Guan, and T. Kürner, "Channel sounding techniques for applications in THz communications: A first correlation based channel sounder for ultra-wideband dynamic channel measurements at 300 GHz," in *Proc. 9th Int. Congr. Ultra Mod. Telecommun. Control Syst. Workshops (ICUMT)*, Munich, Germany, Nov. 2017, pp. 449–453.

[25] T. S. Rappaport, *Wireless Communications Priciples and Practice*, 2nd ed. Upper Saddle River: Prentice-Hall, 2002.

[26] J. Liang, J. Lee, M.-D. Kim, and X. Yin, "Synthesis techniques of narrow beam-width directional antenna measurements for millimeter-wave channel characterization," in *Proc. Int. Conf. Inf. Commun. Technol. Converg. (ICTC)*, Jeju, South Korea, Oct. 2015, pp. 689–693.

[27] B. H. Fleury, "First- and second-order characterization of direction dispersion and space selectivity in the radio channel," *IEEE Trans. Inf. Theory*, vol. 46, no. 6, pp. 2027–2044, Sep. 2000.

[28] W. Fan, F. Zhang, Z. Wang, O. K. Jensen, and G. F. Pedersen, "On angular sampling intervals for reconstructing wideband channel spatial profiles in directional scanning measurements," *IEEE Trans. Veh. Technol.*, vol. 69, no. 11, pp. 13910–13915, Nov. 2020.

[29] B. Peng, S. Rey, D. M. Rose, S. Hahn, and T. Kürner, "Statistical characteristics study of human blockage effect in future indoor millimeter and sub-millimeter wave wireless communications," in *Proc. IEEE 87th Veh. Technol. Conf. (VTC Spring)*, Porto, Portugal, Jun. 2018, pp. 1–5.

[30] J. M. Eckhardt, T. Doeker, S. Rey, and T. Kürner, "Measurements in a real data centre at 300 GHz and recent results," in *Proc. 13th Eur. Conf. Antennas Propag. (EuCAP)*, Krakow, Poland, Mar. 2019, pp. 1–5.

[31] K. Guan *et al.*, "Channel sounding and ray tracing for intrawagon scenario at mmWave and sub-mmWave bands," *IEEE Trans. Antennas Propag.*, vol. 69, no. 2, pp. 1007–1019, Feb. 2021.

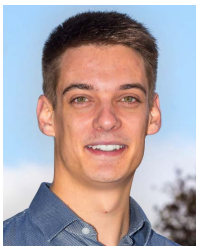

Tobias Doeker (Graduate Student Member, IEEE) was born in Haltern, Germany, in 1994. He received the B.Sc. degree in electrical engineering from the Hamburg University of Applied Science, Hamburg, Germany, in 2017, and the M.Sc. degree in electrical engineering with a focus on communications technology from Technische Universität Braunschweig, Brunswick, Germany, in 2019, where he is currently pursuing the Ph.D. degree.

Besides, he was a Student Trainee at Lufthansa Technik AG, Hamburg, from 2013 to 2019. In November 2019, he joined the Institute for Communications Technology, Technische Universität Braunschweig, as a Researcher. His research interests are focused on the THz communication and here, especially, on radio channel measurements and characterization as well as device discovery for multi gigabit indoor communication at 300 GHz.

Johannes M. Eckhardt (Graduate Student Member, IEEE) was born in Brunswick, Germany, in 1992. He received the Dipl.-Ing. degree in electrical engineering from Technische Universität Dresden, Dresden, Germany, in 2017, and the M.A. degree from the École Centrale Paris, Gif-sur-Yvette, France, in 2017. He is currently pursuing the Ph.D. degree with the Department of Mobile Radio Systems, Institute for Communications Technology, Technische Universität Braunschweig, Brunswick, Germany.

His research interests include channel measurements and modeling, link-level simulations, and interference studies in complex scenarios for multi gigabit communication systems at THz frequencies.

Thomas Kürner (Fellow, IEEE) received the Dipl.-Ing. degree in electrical engineering and the Dr.-Ing. degree from the University of Karlsruhe, Karlsruhe, Germany, in 1990 and 1993, respectively.

From 1990 to 1994, he was with the Institut für Höchstfrequenztechnik und Elektronik (IHE), University of Karlsruhe, working on wave propagation modeling, radio channel characterization, and radio network planning. From 1994 to 2003, he was with the Radio Network Planning Department at the headquarters of the GSM 1800 and UMTS operator E-Plus Mobilfunk GmbH & Company KG, Düsseldorf, Germany, where he was the Team Manager Radio Network Planning Support responsible for radio network planning tools, algorithms, processes, and parameters from 1999 to 2003. Since 2003, he has been a Full University Professor of mobile radio systems with the Technische Universität Braunschweig, Brunswick, Germany. In 2012, he was a Guest Lecturer with Dublin City University, Dublin, Ireland, within the Telecommunications Graduate Initiative in Ireland.

Prof. Dr.-Ing. Kürner is currently chairing the IEEE 802.15 Standing Committee THz. He was also the Chair of IEEE 802.15.3d TG 100G which developed the worldwide first wireless communications standard operating at 300 GHz. He is also the Project Coordinator of the H2020-EU-Japan project ThoR ("TeraHertz end-to-end wireless systems supporting ultra-high data Rate applications") and the Coordinator of the German DFG-Research Unit FOR 2863 Meteracom ("Metrology for THz Communications"). In 2019, he received the Neal-Shephard Award of the IEEE Vehicular Technology Society (VTS). Since 2016, he has been a member of the Board of Directors of the European Association on Antennas and Propagation (EurAAP) and a Distinguished Lecturer of IEEE Vehicular Technology Society since 2020.